Resolution Enhancement for Mixed Boundary Conditions in Inverse Scattering Problems

Fan Yin, *Student Member, IEEE*, Chang Chen, *Member, IEEE*, and Weidong Chen, *Member, IEEE*

***Abstract*— In the mixed boundary inverse scattering problem (ISP), conducting and dielectric scatterers coexist in the same region, which challenges the present quantitative inverse scattering methods. Moreover, to ensure the incident waves penetrating the lossy or high-contrast objects, lower wavelength is applied in most inverse scattering applications. Therefore, methods with wavelength or subwavelength resolution are required for the mixed boundary ISP. In this article, we devise a quantitative inversion scheme alternately updating the contrast of dielectric scatterers and the T-matrix of conducting scatterers. The proposed alternate parameter updating method (APUM) avoids the reconstruction deterioration from both the large imaginary parts of conducting contrasts and the limited expansion order of the T-matrix. Then, we further improve the resolution of the APUM by optimizing the incident fields, which is also a regularization strategy. In particular, we design superoscillatory incident fields to quantitatively converse the high spatial spectrum of objects into low spectrum contrast sources, which can retain the high-frequency information of objects in the low-passband of the Green function. The results with synthetic data and single-frequency Fresnel experimental data verify the effectiveness of the proposed method.**

***Index Terms*— Alternate parameter updating method (APUM), contrast source inversion (CSI), inverse T-matrix method, quantitative inverse scattering problem (ISP), superoscillation.**

I. Introduction

INVERSE scattering problems (ISPs) arise in diverse application areas, such as nondestructive testing [1], [2], biomedical imaging [3], geological exploration [4], through wall imaging [5], and ground penetrating radar [6]. In most of these applications, dielectric and conducting objects exist in the same region, which is a mixed boundary ISP. All these applications require incident wave penetrating observed objects, while the skin effects of these lossy objects limit the wavelength to the scale of objects. To image wavelength scale objects with mixed boundary conditions, achieving superresolution in inverse scattering imaging has always been the focus of the relevant research fields [7]–[9].

In the mixed boundary ISP, qualitative methods reconstruct the shape of scatterers only [10]–[12], of which the information is not enough. The quantitative methods such as the contrast source inversion (CSI) method [13], [14] and the inverse T-matrix method [15] can retrieve the physical properties and distinguish between conducting scatterers and dielectric scatterers. The CSI method solves the problem under electric field integral equation (EFIE) model and approximates the conducting scatterers by lossy dielectric scatterers according to the volume equivalence principle. However, the CSI method may fail in the case with high-loss dielectric scatterers or PEC scatterers where the large imagery components will corrupt the reconstructed results. To overcome these defects, a uniform framework to model the scattering of different types of scatterers is applied to recover the T-matrix coefficients of the scatterers [16]–[19]. Different from the volume equivalence principle used in the EFIE model, the T-matrix model describes scattering by imposing boundary conditions on each discrete pixel with multipole expansion. The contrasts of the dielectric scatterers are obtained from the small term asymptotic approximations for T-matrix [15]. Because the computational cost limits the expansion degrees, the approximations in the inverse T-matrix method are inaccurate. The reconstructions of dielectric scatterers in the inverse T-matrix method cannot achieve the same resolution as CSI. Therefore, a combined method to make advantage of both methods is a possible way to improve the imaging quality.

Compared with the ISP for dielectric objects, the mixed boundary ISP applies lower frequency waves to penetrate the objects and requires higher imaging resolution. Therefore, achieving subwavelength resolution in the quantitative mixed boundary ISP is a problem to be solved. As Green's function in free space is bandlimited with free space wavenumber k_0, the high-frequency information of the induced currents is discarded from the scattering fields [20]. Consequently, the spatial resolution of inverse source problems is limited to π/k_0, which is the Rayleigh resolution limit [8]. From the mathematical perspective, such a compact integral operator with Green's function as the kernel causes the ill-posedness of the ISPs, which results in the solution not depending continuously on the data [21]. Moreover, for scattering fields mapped by the compact Green operator belonging to a compact set, the correlation between each measured data point increases with the number of measurements, which makes the data equation undetermined and ill-conditioned regardless of the number of sensors [22], [23]. Therefore, achieving superresolution and regularization of ill-posed problems have the same end in ISPs.

Manuscript received March 16, 2021; revised September 27, 2021; accepted November 19, 2021. Date of publication December 28, 2021; date of current version May 5, 2022. This work was supported in part by the National Natural Science Foundation of China under Grant 61971392. *(Corresponding author: Chang Chen.)*

The authors are with the Department of Electronics Science and Technology, University of Science and Technology of China, Hefei 230026, China (e-mail: yinfan@mail.ustc.edu.cn; changchen@ustc.edu.cn; wdchen@ustc.edu.cn).

Color versions of one or more figures in this article are available at https://doi.org/10.1109/TAP.2021.3137294.

Digital Object Identifier 10.1109/TAP.2021.3137294

Various types of regularization techniques directly impose constrains on solutions, including the total variation type [24], multiplicative regularization type [25], Bayesian type [26], and sparsity type [27], [28]. Some of these constraints are not universal for practical problems. Other methods make use of the nonlinearity of the ISPs to defeat the ill-posedness [29]–[32]. Compared with linear inverse scattering methods, nonlinear inversion algorithms consider the Lippmann–Schwinger equation in addition and show subwavelength resolution performances [8], [33]. A widely accepted explanation for this superresolution ability is that the conversion of evanescent waves to propagating waves is included in the nonlinear model [8], [34]–[36]. Therefore, the incident field modulating method is proposed to increase the reconstructed information [37]. However, disagreement arises regarding the lack of a convincing quantitative approach to extract the evanescent wave spectrum from the measured propagating wave spectrum [9]. Recent investigation of the superresolution effect in nonlinear inverse scattering gives an unoptimistic solution in which superresolution in nonlinear ISPs is unavailable without priori information [38]. Instead of the inverse source method, the first kind of Born approximation is adopted as the example of linear inverse scattering in [38], which, however, neglects the fact that the Rayleigh limit arises from the inverse source problem instead of the quantitative ISP. The superresolution effects in the nonlinear inverse problem remain controversial.

Since the lack of high-frequency information cannot be remedied by any mathematical technique, most physical superresolution methods attempt to gain access to evanescent waves. Lens, slabs, or metasurfaces are arranged near the objects conversing evanescent waves to propagating waves [39]–[44]. These evanescent-to-propagating wave conversion devices alter the domain of interest (DOI) from free space into space with an inhomogeneous background medium, of which Green's function has wider bandwidth [40], and cast the inverse problem into a well-conditioned equation [41]. However, these approaches are limited to the case of cooperative objects, which is unsuited to most inverse scattering applications. The other categories of physical superresolution methods make use of superoscillation effects without extra equipment. The effect of superoscillation produces oscillations that vary faster than the highest Fourier component of the oscillations [45]. Based on this, incident waves with subwavelength spots achieve superresolution in far fields without contributions from evanescent fields [46]–[51]. Sharing the same principle as Schelkunoff's superdirective arrays, superoscillatory waves come with exponentially growing energy, which makes it a tradeoff between the signal-to-noise ratio (SNR) and the bandwidth [52], [53]. Because the superoscillatory wave only exists in the local segment, prior information for the scale of DOI leads to regularization.

In this article, we treated the mixed boundary ISP as an alternate inversion of the contrast and the T-matrix. Instead of updating the contrast and the T-matrix with the alternating direction multiplier method (ADMM), an alternate parameter updating method (APUM) is proposed to alternately update the contrast of dielectrics and the T-matrix of conductors. APUM avoids the contrast interfered by the large imaginary parts of the conductors and improves the accuracy of the reconstructed T-matrix. To further improve the resolution, we proposed an incident field optimization for quantitatively coupling the high-frequency information of objects into a propagating wave. Superoscillation effects can mix the high-frequency information into bandlimited-induced currents, which is a superoscillatory-to-propagating wave conversion. The conversion mechanism works on quantitative ISP (most nonlinear problems) instead of qualitative ISP (typical linear problems). The singular value decomposition (SVD) of the matrix in the data equation shows that the optimization of the incident fields can increase the singular values. The linear relationship between the data and the incident fields makes the optimization of the incident fields a regularization strategy.

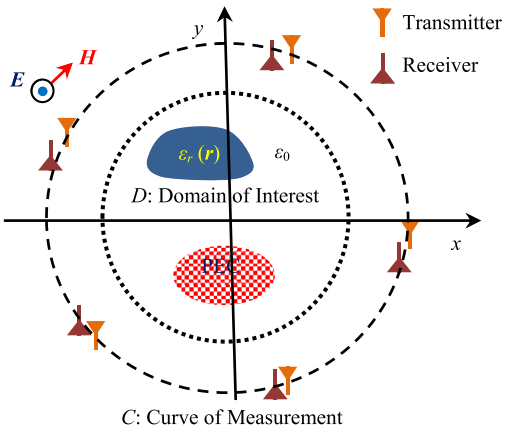

Fig. 1. Geometry for the ISP: the dielectric scatterers with permittivity ε and the PEC scatterers coexist in the DOI.

The main contributions of the proposed methods are as follows: first, the APUM is proposed for mixed boundary conditions, which provides the contrast and the T-matrix with higher accuracy. Second, a quantitative superoscillatory-to-evanescent wave conversion is accomplished by the incident field optimization, which is a regularization strategy and provides a uniform resolution enhancement for the mixed boundary ISP.

This article is organized as follows. Section II contrasts the volume equivalence model and the boundary condition model and combines two models. Section III presents the use of high-frequency information and incident field optimization. Section IV presents the APUM. In Section V, we present the synthetic and experimental results. Conclusions are made in Section VI.

II. Formulation of the Problem

A typical 2-D ISP is shown in Fig. 1.

Region D is the DOI where the probed objects are located, and curve C is where the receivers and transmitters are located. Transmitters emit the single-frequency wave simultaneously, and receivers measure the steady-state scattering field. The cylindrical dielectric scatterers and the cylindrical PEC scatterers with arbitrary cross sections are inhomogeneous in the (x, y) plane but homogeneous along the z-axis. The incident wave is a transverse magnetic (TM) wave, which simplifies the

problem into a scalar equation. The scatterers are nonmagnetic mediums.

A. Volume Equivalence Model

According to the volume equivalence principle, we obtain the data equation and the state equation to describe the imaging problem as a nonlinear problem as

$$\begin{cases} \boldsymbol{E}^{sca}(\boldsymbol{r}_m) = k_0^2 \displaystyle\int_D G_0(\boldsymbol{r}_m, \boldsymbol{r}')\boldsymbol{E}(\boldsymbol{r}')\chi(\boldsymbol{r}')d\boldsymbol{r}' \\ \boldsymbol{E}(\boldsymbol{r}) = \boldsymbol{E}^{inc}(\boldsymbol{r}) + \boldsymbol{E}^{sca}(\boldsymbol{r}) \end{cases} \tag{1}$$

where $\boldsymbol{E}$, $\boldsymbol{E}^{\mathbf{sca}}$, $\boldsymbol{E}^{\mathrm{inc}}$, G_0, k_0, and $\boldsymbol{r}_m$ are the total field, the scattering field, the incident field, the free space Green function, the free space wavenumber, and the position vector of the mth receiver, respectively. $\chi = \varepsilon_r - 1$ is the contrast, where ε_r is the relative permittivity. Introducing the contrast source $\boldsymbol{w} = \boldsymbol{E}\chi$ into it and discrete (1) with the Galerkin method, we obtain the matrix form of the inverse contrast problem as

$$\begin{cases} \boldsymbol{e}_q^{sca} = \boldsymbol{G}_C \cdot \boldsymbol{w}_q \\ \boldsymbol{w}_q = \boldsymbol{\chi} \odot \left(\boldsymbol{e}_q^{inc} + \boldsymbol{G}_D \cdot \boldsymbol{w}_q\right) \end{cases} \tag{2}$$

where subscript q represents the qth illumination, and $\odot$ is the symbol of element-wise multiplication.

B. T-Matrix Model

In the T-matrix model, the DOI is discretized into N small cylindrical elements at first. The center of the nth elements is $\boldsymbol{r}_n$. Then, the field is divided into the incident field $\boldsymbol{E}^{\mathrm{inc}}$ outside of the elements, the scattering field $\boldsymbol{E}^{\mathrm{sca}}$ outside of the elements, and the transmitting fields $\boldsymbol{E}^{\mathrm{trans}}$ inside each of the elements. All the fields can be represented as the form of multipole expansion with different expansion coefficients [16]. The boundary conditions imposed on the surface of the nth element with radius R can be expressed as

$$\left[\boldsymbol{E}^{inc}(\boldsymbol{r}) + \boldsymbol{E}^{sca}(\boldsymbol{r})\right]_{|\boldsymbol{r}-\boldsymbol{r}_n|=R} = \boldsymbol{E}^{trans}(\mathbf{r})\big|_{|\boldsymbol{r}-\boldsymbol{r}_n|=R} \tag{3}$$

while the right components of (3) are zero in the PEC scatterers. The corresponding boundary condition of the magnetic field for the nth element is obtained from the electric field as

$$\left[\frac{\partial \boldsymbol{E}^{inc}(\boldsymbol{r})}{\partial r} + \frac{\partial \boldsymbol{E}^{sca}(\boldsymbol{r})}{\partial r}\right]_{|\boldsymbol{r}-\boldsymbol{r}_n|=R} = \left.\frac{\partial \boldsymbol{E}^{trans}(\boldsymbol{r})}{\partial r}\right|_{|\boldsymbol{r}-\boldsymbol{r}_n|=R}. \tag{4}$$

Solving (3) and (4) (see the Appendix), we obtain the coefficients of scattering field at pth order multipole expansion from the nth element

$$c_{np} = t_n^p \left[i_n^p + \sum_{n'=1}^{N} \sum_{p'=-\infty}^{+\infty} s_{n,n'}^{p,p'} \left(1 - \delta_{n,n'}\right) c_{n'p'} \right] \tag{5}$$

where c_{np} is the pth order multipole expansion of the scattering field at $\boldsymbol{r}_{\mathrm{n}}$, i_n^p is the pth order multipole expansion of the incident field at $\boldsymbol{r}_{\mathrm{n}}$, and $s_{n,n'}^{p,p'}$ is the translation coefficient between the pth order multipole at $\boldsymbol{r}_{\mathrm{n}}$ and p'th order multipole at $\boldsymbol{r}_{n'}$. t_n^p is the transmitting parameter for the boundary condition of the nth element. The transmitting parameter of the dielectric element is

$$t_n^p = \frac{k_n J_p(k_0 R) J_{p+1}(k_n R) - k_0 J_p(k_n R) J_{p+1}(k_0 R)}{k_0 J_p(k_n R) H_{p+1}^{(2)}(k_0 R) - k_n H_p^{(2)}(k_0 R) J_{p+1}(k_n R)} \tag{6}$$

while the PEC element has the parameter

$$t_n^p = -J_p(k_0 R) / H_p^{(2)}(k_0 R). \tag{7}$$

Given the scattering coefficients c_{np}, the scattering field can be expressed as

$$\boldsymbol{E}^{sca}(\boldsymbol{r}) = \boldsymbol{u}_z \sum_{p=-P}^{+P} \sum_{n=1}^{N} c_{np} H_p^{(2)}(k_0|\boldsymbol{r} - \boldsymbol{r}_n|) e^{-jp\varphi(\boldsymbol{r}-\boldsymbol{r}_n)} \tag{8}$$

where $\varphi(\boldsymbol{r} - \boldsymbol{r}_n)$ is the angle of $\boldsymbol{r} - \boldsymbol{r}_n$ in cylindrical coordinate.

For all cylindrical elements, (8) and (5) can be written in matrix form

$$\begin{cases} \boldsymbol{e}_q^{sca} = \boldsymbol{G} \cdot \boldsymbol{c}_q \\ \boldsymbol{c}_q = \boldsymbol{T}\left(\boldsymbol{i}_q + \boldsymbol{S} \cdot \boldsymbol{c}_q\right) \end{cases} \tag{9}$$

where q represents qth illumination, $\boldsymbol{e}_q^{\mathrm{sca}}$ is the vector of the measured scattering field, $\boldsymbol{c}_q$ is the vector of the scattering coefficient, $\boldsymbol{i}_q$ is the vector of the incident field coefficient, $\boldsymbol{S}$ is the translational matrix, and $\boldsymbol{T}$ is the transmitting matrix, known as the T-matrix. Obviously, (9) has a similar formulation to (2). However, (9) is established on the infinite order expansion of multipoles. The truncation of the expansion order p leads to a decrease in the model accuracy. Therefore, inverse T-matrix methods cannot perform as well as inverse contrast methods.

C. Combined Parameter Model

The volume equivalence model cannot handle the conductors for the large imaginary part, while the boundary condition model has the ability to handle different types of scatterers. However, the boundary condition model has less accuracy than the volume equivalence model due to its truncated expansion order. A combined parameter model can benefit from both models.

The data equations in (2)

$$\boldsymbol{G}_C = \left[\frac{k_0^2 \pi R^2}{4j} H_0^{(2)}(k_0|\boldsymbol{r}_m - \boldsymbol{r}_n|)\right]_{M \times N} \tag{10}$$

is similar to the data equations in (9)

$$\boldsymbol{G} = \left[H_n^{(2)}(k_0|\boldsymbol{r}_m - \boldsymbol{r}_n|) e^{-jn\varphi(\boldsymbol{r}_m - \boldsymbol{r}_n)}\right]_{M \times N(2P+1)}. \tag{11}$$

Introducing the data equation in (9) into the data equation in (2), we obtain

$$\boldsymbol{G}_C \cdot \boldsymbol{w}_q = \boldsymbol{G} \cdot \boldsymbol{c}_q. \tag{12}$$

For the truncation number $p = 0$, the scattering coefficients are linear to the contrast sources

$$\boldsymbol{c}_q = j \frac{k_0^2 \pi R^2}{4} \boldsymbol{w}_q. \tag{13}$$

Therefore, the volume equivalence model and the T-matrix model share the same data equation, and the combined parameter model is

$$\begin{cases} \boldsymbol{e}_q^{sca} = \boldsymbol{G}_C \cdot \boldsymbol{w}_q \\ \boldsymbol{w}_q = \boldsymbol{\chi} \odot \left(\boldsymbol{e}_q^{inc} + \boldsymbol{G}_D \cdot \boldsymbol{w}_q\right) \\ \boldsymbol{w}_q = \boldsymbol{T}\left(-j\dfrac{\eta_0}{4\pi R^2}\boldsymbol{i}_q + \boldsymbol{S}\cdot\boldsymbol{w}_q\right). \end{cases} \tag{14}$$

In principle, the T-matrix model with smaller mesh size and higher multipole expansion orders has higher accuracy. However, with given tolerance, the accuracy of the T-matrix model can trade off the expansion orders against the scale of mesh grids. Therefore, the multipole expansion at the 0th order works for the most cases at the cost of finer mesh grids.

Because the truncation number of the multipole expansion in (14) is $p = 0$, the difference between the dielectric scatterers and the PEC scatterers is the real part of the elements in the T-matrix. Appling asymptotic approximations of Bessel functions to (6) and (7) at zero order, we have

$$t_n^0 \approx \begin{cases} -j\dfrac{\pi (k_0 R)^2}{4}[1-\varepsilon_r(\boldsymbol{r}_n)], & \text{dielectric} \\ -\left[\dfrac{\pi}{2\ln(2/\gamma\, k_0 R)}\right]^2 + j\dfrac{\pi}{2\ln(2/\gamma\, k_0 R)}, & \text{PEC} \end{cases} \tag{15}$$

where $\gamma \approx 1.78$. Thanks to the observation, the scatterers could be classified as being metallic or dielectric. In (15), the dielectric elements of the T-matrix have positive imaginary parts, while the PEC elements have negative imaginary parts.

III. Solution Method of Inversion Problem

With the given combined model, the inversion method for the mixed boundary ISP is studied in this section. Solving (14) can be formulated as the following optimization problem:

$$\begin{aligned} &\min \frac{\sum_q \left\|\boldsymbol{\gamma}_q\right\|_2^2}{\sum_q \left\|\boldsymbol{\chi} \odot \boldsymbol{e}_q^{inc}\right\|_2^2} + \frac{\sum_q \left\|\boldsymbol{\varsigma}_q\right\|_2^2}{\sum_q \left\|-j\eta_0 \boldsymbol{T}\boldsymbol{i}_q/4\pi R^2\right\|_2^2} \\ &\text{s.t. } \boldsymbol{e}_q^{sca} = \boldsymbol{G}_C \cdot \boldsymbol{w}_q \quad q = 1, \ldots, Q \end{aligned} \tag{16}$$

where γ_q and ς_q are the state errors of (14) defined as

$$\begin{aligned} \boldsymbol{\gamma}_q &= \boldsymbol{\chi} \odot \left(\boldsymbol{e}_q^{inc} + \boldsymbol{G}_D \boldsymbol{w}_q\right) - \boldsymbol{w}_q \\ \boldsymbol{\varsigma}_q &= \boldsymbol{T}\left(-j\frac{\eta_0}{4\pi R^2}\boldsymbol{i}_q + \boldsymbol{S}\boldsymbol{w}_q\right) - \boldsymbol{w}_q. \end{aligned} \tag{17}$$

Equation (16) can be solved by ADMM. However, the relationship between $\boldsymbol{\chi}$ and $\boldsymbol{T}$ is only established on the multipole expansion at zero order, which limits the accuracy of the reconstructed T-matrix. Moreover, in the mixed boundary ISP, the infinite imaginary part of $\boldsymbol{\chi}$ for PEC scatterers corrupts the real part of $\boldsymbol{\chi}$ for dielectric scatterers. To avoid these defects, updating $\boldsymbol{\chi}$ and $\boldsymbol{T}$ is divided into updating for dielectric scatterers and PEC scatterers alternately.

A. Initial Guess of the Boundary Conditions

To reconstruct dielectric scatterers and PEC scatterers, an initial guess of the boundary conditions is provided by the inverse T-matrix, which can be formulated as the cost function

$$f\left(\boldsymbol{w}_q, \boldsymbol{T}\right) = \frac{\sum_q \left\|\boldsymbol{r}_q\right\|_2^2}{\sum_q \left\|\boldsymbol{e}_q^{sca}\right\|_2^2} + \frac{\sum_q \left\|\boldsymbol{\varsigma}_q\right\|_2^2}{\sum_q \left\|-j\eta_0 \boldsymbol{T}\boldsymbol{i}_q/4\pi R^2\right\|_2^2} \tag{18}$$

where $\boldsymbol{r}_q$ is the data error defined as

$$\boldsymbol{r}_q = \boldsymbol{e}_q^{sca} - \boldsymbol{G}_C \boldsymbol{w}_q. \tag{19}$$

Minimization of (18) can be solved by the Polak–Ribière–Polyak (PRP) conjugate gradient method. Since the PRP conjugate gradient method has a strong global convergence property for the most unconstrained convex problems, the initial value of $\boldsymbol{w}_q$ can simply be determined by the back propagation method. Assuming $\boldsymbol{w}_{q,n-1}$ and T_{n-1} are known, $\boldsymbol{w}_{q,n}$ is updated by

$$\boldsymbol{w}_{q,n} = \boldsymbol{w}_{q,n-1} + a_{q,n}\boldsymbol{v}_{q,n}. \tag{20}$$

$\boldsymbol{v}_{q,n}$ is the PRP conjugate gradient direction

$$\begin{cases} \boldsymbol{v}_{q,0} = 0 \\ \boldsymbol{v}_{q,n} = \boldsymbol{g}_{q,n} + \dfrac{\left\langle \boldsymbol{g}_{q,n}, \boldsymbol{g}_{q,n} - \boldsymbol{g}_{q,n-1}\right\rangle}{\left\langle \boldsymbol{g}_{q,n-1}, \boldsymbol{g}_{q,n-1}\right\rangle}\boldsymbol{v}_{q,n-1} \end{cases} \tag{21}$$

where

$$\boldsymbol{g}_{q,n} = -\frac{\boldsymbol{G}_c^H \boldsymbol{r}_{q,n-1}}{\sum_q \left\|\boldsymbol{e}_q^{sca}\right\|_2^2} + \frac{\boldsymbol{\varsigma}_{q,n-1} - \left(\boldsymbol{T}_{n-1}\boldsymbol{S}\right)^H \boldsymbol{\varsigma}_{q,n-1}}{\sum_q \left\|-j\eta_0 \boldsymbol{T}_{n-1}\boldsymbol{i}_q/4\pi R^2\right\|_2^2}. \tag{22}$$

$\boldsymbol{a}_{q,n}$ is the exact line search step width

$$\begin{aligned} a_{q,n} = &\left[\frac{\boldsymbol{v}_{q,n}^H \cdot \boldsymbol{G}_C^H \boldsymbol{r}_{q,n-1}}{\sum_q \left\|\boldsymbol{e}_q^{sca}\right\|_2^2} - \frac{\left(\boldsymbol{v}_{p,n} - \boldsymbol{T}_{n-1}\boldsymbol{S}\cdot\boldsymbol{v}_{q,n}\right)^H \boldsymbol{\varsigma}_{q,n-1}}{\sum_q \left\|-j\eta_0 \boldsymbol{T}_{n-1}\boldsymbol{i}_q/4\pi R^2\right\|_2^2}\right] \\ &\cdot \left[\frac{\left\|\boldsymbol{G}_C \boldsymbol{v}_{q,n}\right\|_2^2}{\sum_q \left\|\boldsymbol{e}_q^{sca}\right\|_2^2} + \frac{\left\|\boldsymbol{v}_{q,n} - \boldsymbol{T}_{n-1}\boldsymbol{S}\cdot\boldsymbol{v}_{q,n}\right\|_2^2}{\sum_q \left\|-j\eta_0 \boldsymbol{T}_{n-1}\boldsymbol{i}_q/4\pi R^2\right\|_2^2}\right]^{-1}. \end{aligned} \tag{23}$$

Once $\boldsymbol{w}_{q,n}$ is determined, $\boldsymbol{T}_{\mathrm{n}}$ is obtained by

$$\boldsymbol{T}_n = \operatorname{diag}\left\{\frac{\sum_q \overline{\left(\boldsymbol{i}_q + \boldsymbol{S}\boldsymbol{w}_{q,n}\right)} \odot \boldsymbol{w}_{q,n}}{\sum_q \overline{\left(\boldsymbol{i}_q + \boldsymbol{S}\boldsymbol{w}_{q,n}\right)} \odot \left(\boldsymbol{i}_q + \boldsymbol{S}\boldsymbol{w}_{q,n}\right)}\right\}. \tag{24}$$

With the reconstructed T-matrix, the initial guess of the boundary condition is derived according to (15). The real parts of dielectric scatterers are zeros, while the real parts of PEC scatterers are smaller than zeros.

Because the aforementioned methods are established on the multipole expansion order $p = 0$, $\boldsymbol{S}$ is an $N \times N$ dimension Toeplitz matrix in this case. The multiplication between $\boldsymbol{S}$ and any $N \times 1$ dimension vector can be reformulated as

$$\begin{bmatrix} y_1 \\ \vdots \\ y_N \\ y_{N-1} \\ \vdots \\ y_2 \end{bmatrix} = IFFT\left\{FFT\begin{bmatrix} s_1 \\ \vdots \\ s_N \\ s_{N-1} \\ \vdots \\ s_2 \end{bmatrix} FFT\begin{bmatrix} x_1 \\ \vdots \\ x_N \\ x_{N-1} \\ \vdots \\ x_2 \end{bmatrix}\right\} \tag{25}$$

which simplifies N^2 points multiplication to $2N$ points multiplication and reduces the calculation amount effectively.

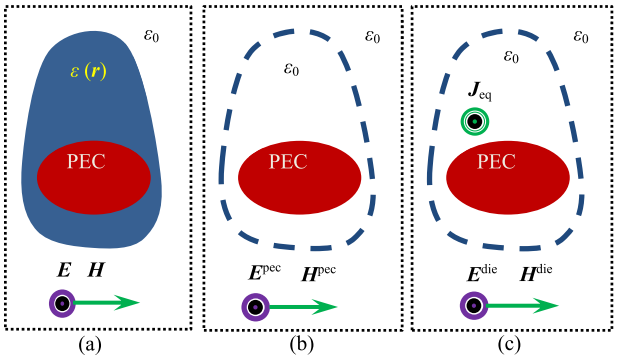

Fig. 2. Geometry for the volume equivalence model with PEC background: (a) original problem; (b) object-free problem; and (c) equivalent problem.

B. Volume Equivalence Model With PEC Background

To handle the mixed boundary problem, we reconstruct the contrast of the dielectric scatterers and the T-matrix of the PEC scatterers alternately. The contrast of the dielectric scatterers is reconstructed in this section, while the T-matrix of the PEC scatterers is acquired from the initial guess or the last step iteration. Since PEC scatterers are obtained from the real parts of the T-matrix, the PEC scatterers are treated as the known background of the volume equivalence model, which avoids the influence of the infinite imaginary part of the contrasts for PEC scatterers.

The original problem is shown in Fig. 2(a). $\boldsymbol{E}$ and $\boldsymbol{H}$ are the electric and magnetic total fields. The Maxwell equation in the original problem is

$$\begin{cases} \nabla \times \boldsymbol{H} = j\omega\varepsilon \boldsymbol{E} \\ \nabla \times \boldsymbol{E} = -j\omega\mu_0 \boldsymbol{H} \end{cases} \tag{26}$$

where

$$\varepsilon(\boldsymbol{r}) = \begin{cases} \varepsilon_r\varepsilon_0, & \boldsymbol{r} \in \text{dielectric} \\ \varepsilon_0, & \boldsymbol{r} \in \text{free space} \\ \varepsilon_0 - j\sigma/\omega, & \boldsymbol{r} \in \text{PEC}. \end{cases} \tag{27}$$

σ is the electrical conductivity. In the case with low-frequency wave, the conductor scatterers can be treated as PEC scatterers of which σ is infinite. However, for good accordance with the practice, we still assign σ a value in the numerical simulation.

The dielectric object-free problem in Fig. 2(b) consists of PEC scatterers only, of which the electric and magnetic total fields are $\boldsymbol{E}^{\text{pec}}$ and $\boldsymbol{H}^{\text{pec}}$. The dielectric object-free problem is formulated as

$$\begin{cases} \nabla \times \boldsymbol{H}^{\text{pec}} = j\omega\varepsilon^{\text{pec}} \boldsymbol{E}^{\text{pec}} \\ \nabla \times \boldsymbol{E}^{\text{pec}} = -j\omega\mu_0 \boldsymbol{H}^{\text{pec}} \end{cases} \tag{28}$$

where

$$\varepsilon_{\text{pec}}(\boldsymbol{r}) = \begin{cases} \varepsilon_0 - j\sigma/\omega, & \boldsymbol{r} \in \text{PEC} \\ \varepsilon_0, & \boldsymbol{r} \in \text{other}. \end{cases} \tag{29}$$

The original problem minus the dielectric object-free problem is

$$\begin{cases} \nabla \times (\boldsymbol{H} - \boldsymbol{H}^{\text{pec}}) = j\omega\left[\varepsilon \boldsymbol{E} - \varepsilon^{\text{pec}} \boldsymbol{E}^{\text{pec}}\right] \\ \nabla \times (\boldsymbol{E} - \boldsymbol{E}^{\text{pec}}) = -j\omega\mu_0 (\boldsymbol{H} - \boldsymbol{H}^{\text{pec}}). \end{cases} \tag{30}$$

Defining $\boldsymbol{H}^{\text{die}} = \boldsymbol{H} - \boldsymbol{H}^{\text{pec}}$ and $\boldsymbol{E}^{\text{die}} = \boldsymbol{E} - \boldsymbol{E}^{\text{pec}}$, we obtain the total fields of the equivalent problem in Fig. 2(c), which can be formulated as

$$\begin{cases} \nabla \times \boldsymbol{H}^{\text{die}} = \boldsymbol{J}^{\text{die}} + j\omega\varepsilon^{\text{pec}} \boldsymbol{E}^{\text{die}} \\ \nabla \times \boldsymbol{E}^{\text{die}} = -j\omega\mu_0 \boldsymbol{H}^{\text{die}}. \end{cases} \tag{31}$$

Introducing (30) into (31), we obtain

$$\boldsymbol{J}^{\text{die}} = j\omega\varepsilon_0 \boldsymbol{E} \chi^{\text{die}} \tag{32}$$

where $\chi^{\text{die}} = \varepsilon_r - 1$. EFIE of (31) is

$$\boldsymbol{E}^{die}(\boldsymbol{r}) = k_0^2 \int_D G_{pec}(\boldsymbol{r}, \boldsymbol{r}') \chi^{die}(\boldsymbol{r}') \boldsymbol{E}(\boldsymbol{r}') d\boldsymbol{r}' \tag{33}$$

of which G_{pec} is the Green function with the PEC scatterer background. Equation (33) is discrete with the Galerkin method as

$$\boldsymbol{e}^{\text{die}} = \boldsymbol{G}_D^{\text{pec}} (\boldsymbol{\chi}^{\text{die}} \odot \boldsymbol{e}). \tag{34}$$

According to the relationship between the Green function and the total field of the Dirac source, the scattering matrix is determined by

$$\boldsymbol{G}_D^{\text{pec}} \approx \left[j\pi\omega^2 R^2 \varepsilon_0 E_{\boldsymbol{r}_{n'}}^{\text{pec}}(\boldsymbol{r}_n) \right]_{N \times N} \tag{35}$$

where $E_{\boldsymbol{r}_{n'}}^{\text{pec}}$ is the total field of the Dirac source at $\boldsymbol{r}_{n'}$. For the T-matrix of PEC scatterers determined in the initial guess, the total field is obtained via (9) as

$$E_{\boldsymbol{r}_{n'}}^{\text{pec}}(\boldsymbol{r}_n) = \boldsymbol{e}_{n'}^{inc} - j\frac{\eta_0}{4\pi R^2} \boldsymbol{G}_C \cdot (\boldsymbol{I} - \boldsymbol{TS})^{-1} \boldsymbol{T} \boldsymbol{i}_{n'}. \tag{36}$$

Therefore, the ISP with a given PEC background is formulated as

$$\begin{cases} \boldsymbol{e}_q^{\text{die}} = \boldsymbol{G}_C^{\text{pec}} \boldsymbol{w}_q^{\text{die}} \\ \boldsymbol{w}_q^{\text{die}} = \boldsymbol{\chi}^{\text{die}} \odot \left(\boldsymbol{e}_q^{\text{pec}} + \boldsymbol{G}_D^{\text{pec}} \boldsymbol{w}_q^{\text{die}} \right) \end{cases} \tag{37}$$

where

$$\boldsymbol{w}_q = \boldsymbol{w}_q^{\text{die}} + \boldsymbol{w}_q^{\text{pec}}. \tag{38}$$

χ^{die} is determined to minimize the cost function

$$g(\boldsymbol{w}_q^{die}, \boldsymbol{\chi}^{die}) = \frac{\sum_q \|\boldsymbol{\gamma}_q\|_2^2}{\sum_q \|\boldsymbol{\chi}^{\text{die}} \odot \boldsymbol{e}_q^{\text{pec}}\|_2^2} + \frac{\sum_q \|\boldsymbol{r}_q^{\text{die}}\|_2^2}{\sum_q \|\boldsymbol{e}_q^{\text{die}}\|_2^2} \tag{39}$$

where $\boldsymbol{r}_q^{\text{die}}$ is the data error defined as

$$\boldsymbol{r}_q^{\text{die}} = \boldsymbol{e}_q^{sca} - \boldsymbol{G}_C \boldsymbol{w}_q^{\text{die}}. \tag{40}$$

Equation (39) is minimized by the conjugate gradient method as well. The initial value of $\boldsymbol{w}_q^{\text{die}}$ is determined by the results of (20) as

$$w_{q,0}^{die}(\boldsymbol{r}) = \begin{cases} w_q(\boldsymbol{r}), & \text{Re}\{T(\boldsymbol{r})\} = 0 \\ 0, & \text{Re}\{T(\boldsymbol{r})\} < 0. \end{cases} \tag{41}$$

Updating of $\boldsymbol{w}_q^{\text{die}}$ is

$$\boldsymbol{w}_{q,n}^{die} = \boldsymbol{w}_{q,n-1}^{die} + a_{q,n} \boldsymbol{v}_{q,n} \tag{42}$$

of which $\boldsymbol{v}_{q,n}$ is the PRP conjugate gradient direction. The conjugate gradient of $\boldsymbol{w}_q^{\text{die}}$ is

$$\boldsymbol{g}_{q,n} = -\frac{\boldsymbol{G}_C^H \boldsymbol{r}_{q,n-1}}{\sum_q \left\|\boldsymbol{e}_q^{die}\right\|^2} + \frac{\boldsymbol{G}_D^H\left(\overline{\boldsymbol{\chi}^{\text{die}}} \odot \boldsymbol{\gamma}_q\right) - \boldsymbol{\gamma}_q}{\sum_p \left\|\boldsymbol{\chi}^{\text{die}} \odot \boldsymbol{e}_q^{\text{pec}}\right\|^2}. \tag{43}$$

$\boldsymbol{a}_{q,n}$ is the exact step width

$$\begin{aligned} a_{q,n} &= \left[\frac{\boldsymbol{v}_{q,n}^H \cdot \boldsymbol{G}_C^H \boldsymbol{r}_{q,n-1}}{\sum_p \left\|\boldsymbol{e}_q^{die}\right\|_2^2} - \frac{\left(\boldsymbol{\chi}_{n-1}^{die} \odot \boldsymbol{G}_D \boldsymbol{v}_{p,n} - \boldsymbol{v}_{p,n}\right)^H \boldsymbol{\gamma}_{q,n-1}}{\sum_p \left\|\boldsymbol{\chi}_{n-1}^{die} \odot \boldsymbol{e}_q^{pec}\right\|_2^2}\right] \\ &\cdot \left[\frac{\left\|\boldsymbol{G}_C \boldsymbol{v}_{q,n}\right\|_2^2}{\sum_p \left\|\boldsymbol{e}_q^{die}\right\|_2^2} + \frac{\left\|\boldsymbol{\chi}_{n-1}^{die} \odot \boldsymbol{G}_D \boldsymbol{v}_{p,n} - \boldsymbol{v}_{p,n}\right\|_2^2}{\sum_p \left\|\boldsymbol{\chi}_{n-1}^{die} \odot \boldsymbol{e}_q^{pec}\right\|_2^2}\right]^{-1}. \end{aligned} \tag{44}$$

Once $\boldsymbol{w}_q^{\text{die}}$ is determined, χ^{die} is obtained by

$$\begin{aligned} \text{Re}\left\{\chi^{die}(\boldsymbol{r})\right\} &= -\frac{\sum_q \text{Re}\left\{w_q^{die}(\boldsymbol{r}) E_q(\boldsymbol{r})\right\}}{\sum_q |E_q(\boldsymbol{r})|^2} \\ \text{Im}\left\{\chi^{die}(\boldsymbol{r})\right\} &= -\frac{\sum_q \text{Im}\left\{w_q^{die}(\boldsymbol{r}) E_q(\boldsymbol{r})\right\}}{\sum_q |E_q(\boldsymbol{r})|^2}. \end{aligned} \tag{45}$$

In this way, the PEC scatterers are treated as a background medium, which constrains the solution space of the dielectric scatterers.

C. Alternate Updating

The contrast sources are divided into $\boldsymbol{w}_q^{\text{pec}}$ for PEC scatterers and $\boldsymbol{w}_q^{\text{die}}$ for dielectric scatterers. Given the two portions of the contrast sources, inversion (14) can be carried out as minimization of the cost function

$$L\left(\boldsymbol{w}_q^{\text{pec}}, \boldsymbol{w}_q^{\text{die}}, \boldsymbol{T}, \boldsymbol{\chi}^{\text{die}}\right) = f\left(\boldsymbol{w}_q^{\text{pec}}, \boldsymbol{T}\right) + g\left(\boldsymbol{w}_q^{\text{die}}, \boldsymbol{\chi}^{\text{die}}\right). \tag{46}$$

The alternate updating of the contrast sources has the form

$$\begin{cases} \boldsymbol{w}_{q,k}^{\text{pec}} = \arg\min\limits_{\boldsymbol{w}_q^{\text{pec}}} \; L\left(\boldsymbol{w}_q^{\text{pec}}, \boldsymbol{w}_{q,k-1}^{\text{die}}, \boldsymbol{T}_{k-1}, \boldsymbol{\chi}_{k-1}^{\text{die}}\right) \\ \boldsymbol{T}_k = \arg\min\limits_{\boldsymbol{T}} \; L\left(\boldsymbol{w}_{q,k}^{\text{pec}}, \boldsymbol{w}_{q,k-1}^{\text{die}}, \boldsymbol{T}, \boldsymbol{\chi}_{k-1}^{\text{die}}\right) \\ \boldsymbol{w}_{q,k}^{\text{die}} = \arg\min\limits_{\boldsymbol{w}_q^{\text{die}}} \; L\left(\boldsymbol{w}_{q,k}^{\text{pec}}, \boldsymbol{w}_q^{\text{die}}, \boldsymbol{T}_{k-1}, \boldsymbol{\chi}_{k-1}^{\text{die}}\right) \\ \boldsymbol{\chi}_k^{\text{die}} = \arg\min\limits_{\boldsymbol{\chi}^{\text{die}}} \; L\left(\boldsymbol{w}_{q,k}^{\text{pec}}, \boldsymbol{w}_{q,k}^{\text{die}}, \boldsymbol{T}_k, \boldsymbol{\chi}^{\text{die}}\right). \end{cases} \tag{47}$$

For $\boldsymbol{w}_q^{\text{pec}}$ and $\boldsymbol{w}_q^{\text{die}}$ independent of each other, minimization of L with respect to $\boldsymbol{w}_q^{\text{pec}}$ or $\boldsymbol{w}_q^{\text{die}}$ equals the minimization of f ($\boldsymbol{w}_q^{\text{pec}}$) or g ($\boldsymbol{w}_q^{\text{die}}$). Therefore, each step of updating in (47) remains the same as the aforementioned modified conjugate gradient method.

Thus, the contrast of the dielectric scatterers and the T-matrix of the PEC scatterers are updated alternately, which improves the quantitative reconstruction of the mixed boundary ISP. However, lossy objects limit the available wavelength to the scale of imaged objects. The wavelength in the mixed boundary ISP is much longer than the ones in the ISP with dielectric scatterers only, which leads to the demand for higher resolution. Therefore, the incident field optimization is proposed as a regularization strategy to further improve the performance of the APUM.

IV. Optimization of Incident Fields

Introducing the two state equations of (14) into the data equation, we obtain

$$\begin{cases} \boldsymbol{e}_q^{sca} = \boldsymbol{G}_C \cdot (\boldsymbol{I} - \boldsymbol{\chi} \odot \boldsymbol{G}_D)^{-1} \boldsymbol{e}_q^{inc} \odot \boldsymbol{\chi} \\ \boldsymbol{e}_q^{sca} = -j\dfrac{\eta_0}{4\pi R^2} \boldsymbol{G}_C \cdot (\boldsymbol{I} - \boldsymbol{TS})^{-1} \boldsymbol{T} \boldsymbol{i}_q \end{cases} \tag{48}$$

where $(\boldsymbol{I} - \boldsymbol{\chi} \odot \mathbf{G}_{\text{D}})^{-1} \boldsymbol{e}_q^{\text{inc}}$ is the total field $\boldsymbol{e}_q$, and $(\boldsymbol{I} - \boldsymbol{TS})^{-1} \boldsymbol{i}_q$ is the multipole expansion coefficients of the total field. Equation (48) exposes the nonlinearity of the inverse problem.

A. Ill-Posedness of the Problem

In (48), $\boldsymbol{G}_c$ is a compact operator, of which the point spectrum converges to zero. The small singular values of $\boldsymbol{G}_c$ make it noninvertible, and the data equation in (14) is an ill-posed problem. The spatial spectrum of the free space Green function is

$$\begin{aligned} \tilde{G}(\boldsymbol{k}) &= \int_{-\infty}^{+\infty} \int_0^{2\pi} G_0(\boldsymbol{r}) e^{-j\boldsymbol{k}\cdot\boldsymbol{r}} d\boldsymbol{r} \\ &= -\frac{j\pi}{2} \lim_{x\to\infty} \int_{-\infty}^{+\infty} r H_0^{(2)}(k_0 r) J_0(k_r r) dr \\ &\approx \frac{-j}{2k_0} \delta(k_r - k_0) \end{aligned} \tag{49}$$

which shows the spatial spectrum of $\boldsymbol{G}_c$ limited to k_0. As a consequence, the high spatial spectrum of $\boldsymbol{w}_q$ is cut off from the scattering field, which limits the resolution of $\boldsymbol{w}_q$ to the Rayleigh limit π/k_0.

In (48), $\boldsymbol{TS}$ and $\boldsymbol{\chi} \odot \mathbf{G}_{\text{D}}$ are also compact operators. According to the Fredholm alternative theorem, $(\boldsymbol{I} - \boldsymbol{TS})^{-1}$ and $(\boldsymbol{I} - \boldsymbol{\chi} \odot \boldsymbol{G}_{\text{D}})^{-1}$ are regular operator for any $\boldsymbol{T}$ and $\boldsymbol{\chi}$. Therefore, $\boldsymbol{T}$ and $\boldsymbol{\chi}$ have no significant impact on the distribution of the singular values for $(\boldsymbol{I} - \boldsymbol{TS})^{-1}$ and $(\boldsymbol{I} - \boldsymbol{\chi} \odot \mathbf{G}_{\text{D}})^{-1}$. With given incident fields, the ill-posedness does not change with the objects. Therefore, $(\boldsymbol{I} - \boldsymbol{\chi} \odot \mathbf{G}_{\text{D}})^{-1} \boldsymbol{e}_q^{\text{inc}} \odot \boldsymbol{\chi}$ and $(\boldsymbol{I} - \boldsymbol{TS})^{-1} \boldsymbol{T} \boldsymbol{i}_q$ share the same solution spaces with $\boldsymbol{e}_q^{\text{inc}} \odot \boldsymbol{\chi}$ and $\boldsymbol{T} \boldsymbol{i}_q$. Similar conclusion is obtained in [38], where the solution space of the fully nonlinear scheme is not better than the one of the first order Born approximation scheme. Hence, the resolution of $\boldsymbol{e}_q^{\text{inc}} \odot \boldsymbol{\chi}$ and $\boldsymbol{T} \boldsymbol{i}_q$ is also maintained at π/k_0. Given the spectrum limits of $\boldsymbol{e}_q^{\text{inc}} \odot \boldsymbol{\chi}$ and $\boldsymbol{T} \boldsymbol{i}_q$, the available spectra of $\boldsymbol{\chi}$ and $\boldsymbol{T}$ depend on the incident fields.

Therefore, optimization of the incident fields is a key to retain high-frequency information of objects in the scattering fields.

B. Superoscillatory-to-Propagating Wave Conversion

In computational imaging methods, knowledge of incident fields is indispensable. Although the spectra of $\boldsymbol{\chi} \odot \boldsymbol{e}_q^{inc}$ and $\boldsymbol{T} \boldsymbol{i}_q$ are limited by the Green function $\boldsymbol{G}_c$, the spectra of $\boldsymbol{\chi}$ and $\boldsymbol{T}$ depend on both the incident fields and the Green function, which can be improved by optimization for incident fields. The relationship between the spectra of scattering fields and

the spectra of contrasts is

$$\tilde{\boldsymbol{E}}_q^{sca}(\boldsymbol{k}) = k_0^2 \tilde{G}_0(\boldsymbol{k}) \int_{\infty} \boldsymbol{E}_q(\boldsymbol{r}')\chi(\boldsymbol{r}')\Gamma_D(\boldsymbol{r}')e^{-j\boldsymbol{k}\cdot\boldsymbol{r}'}d\boldsymbol{r}' = k_0^2 \tilde{G}_0(\boldsymbol{k})\tilde{\boldsymbol{w}}_q(\boldsymbol{k}) \tag{50}$$

where Γ_D is the characteristic function of region D. $\boldsymbol{w}_q$ is the mixing between $\boldsymbol{\chi}$ and $\boldsymbol{E}_q\Gamma_D$. Moreover, the uniqueness of $(\boldsymbol{I} - \boldsymbol{\chi} \odot \mathbf{G}_{\mathrm{D}})^{-1}$ indicates that the bandwidth of $\boldsymbol{w}_q$ depends on the mixing between $\boldsymbol{\chi}$ and $\boldsymbol{E}_q^{inc}\Gamma_D$.

According to superoscillation theory, the waveform over particular intervals shows local oscillations with an arbitrary frequency outside the frequency range of the waveform [34]. The spectrum of the local incident fields $\boldsymbol{E}_q^{inc}\Gamma_D$ can be designed to mix a specific high spatial spectrum of $\boldsymbol{\chi}$ into the low-passband of the Green function. The multipole expansion at the coordinate origin of the incident field is as follows:

$$\boldsymbol{E}^{inc}(\boldsymbol{r}) = \boldsymbol{u}_z \sum_{p=-\infty}^{+\infty} \begin{bmatrix} J_p(k_0 r)e^{-jp\varphi(\boldsymbol{r})} \\ \sum_{i=1}^{I}\sum_{\gamma=-\tau}^{+\tau} a_{\gamma i}(q)H_{\gamma+p}^{(2)}(k_0 r_i) \\ e^{j(\gamma+p)\varphi(\boldsymbol{r}_i)}e^{j\gamma\pi} \end{bmatrix} = \boldsymbol{u}_z \sum_{p=-\infty}^{+\infty} \left[J_p(k_0 r)e^{-jp\varphi(\boldsymbol{r})}F_p(q)\right]. \tag{51}$$

The spectrum of the mixing between $\boldsymbol{\chi}$ and $\boldsymbol{E}_q^{\mathrm{inc}}\Gamma_D$ is

$$\int_D \boldsymbol{E}_q^{inc}(\boldsymbol{r}')\chi(\boldsymbol{r}')e^{-j\boldsymbol{k}\cdot\boldsymbol{r}'}d\boldsymbol{r}' = \sum_{p=-\infty}^{+\infty} F_p(q)\int_D J_p(k_0 r')e^{-jp\varphi'}\chi(\boldsymbol{r}')e^{-j\boldsymbol{k}\cdot\boldsymbol{r}'}d\boldsymbol{r}'. \tag{52}$$

For the convenience of derivation, the DOI is circular with radius R_D. Supposing the spectrum of the contrast is $\boldsymbol{k}_{\mathrm{q}}$, the contrast is

$$\chi(\boldsymbol{r}) = e^{-j\boldsymbol{k}_q\cdot\boldsymbol{r}}. \tag{53}$$

By substituting (52) and (53) into (51), the mixing spectrum can be expressed as

$$\begin{aligned}\int_D \boldsymbol{E}_q^{inc}(\boldsymbol{r}')\chi(\boldsymbol{r}')e^{-j\boldsymbol{k}\cdot\boldsymbol{r}'}d\boldsymbol{r}' &= \sum_{p=-\infty}^{+\infty}\begin{bmatrix} F_p(q)e^{-jp[\varphi(\boldsymbol{k}_q)-\pi/2]} \\ \int_0^{R_D} J_p(k_0 r')J_p(k_q r')r'dr' \end{bmatrix} \\ &= \sum_{p=-\infty}^{+\infty}\begin{Bmatrix} F_p(q)e^{-jp[\varphi(\boldsymbol{k}_q)-\pi/2]}\dfrac{R_D}{k_0^2-k_q^2} \\ \begin{bmatrix} k_0 J_p(k_q R_D)J_{p+1}(k_0 R_D) \\ -k_p J_p(k_0 R_D)J_{p+1}(k_q R_D)\end{bmatrix}\end{Bmatrix}\end{aligned} \tag{54}$$

where $k_q \neq k_0$. In the case $k_q = k_0$, the mixing spectrum is

$$\int_D \boldsymbol{E}_q^{inc}(\boldsymbol{r}')\chi(\boldsymbol{r}')e^{-j\boldsymbol{k}\cdot\boldsymbol{r}'}d\boldsymbol{r}' = \sum_{p=-\infty}^{+\infty}\begin{Bmatrix} F_p(q)e^{-jp[\varphi(\boldsymbol{k}_q)-\pi/2]}\dfrac{R_D^2}{2} \\ \begin{Bmatrix}\left[J_p'(k_0 R_D)\right]^2 \\ +\left(1-\dfrac{p^2}{k_0^2 R_D^2}\right)J_p^2(k_q R_D)\end{Bmatrix}\end{Bmatrix}. \tag{55}$$

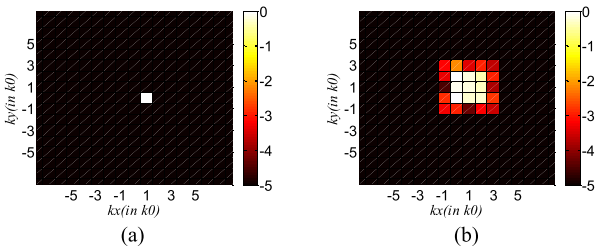

Fig. 3. Spectra of: (a) incident field excited by uniform line sources and (b) sum of incident fields excited by optimized line sources.

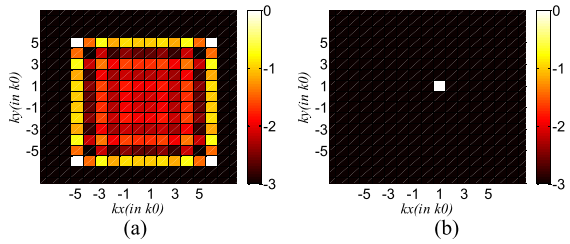

Fig. 4. Spectrum of: (a) sum of contrast sources excited by uniform sources and (b) sum of contrast sources excited by optimized sources.

For F_p being linear to $\alpha_{\gamma i}$, (54) can be discretized by truncating the multipole expansion to order P as follows:

$$\int_D \boldsymbol{E}_q^{inc}(\boldsymbol{r}')\chi(\boldsymbol{r}')e^{-j\boldsymbol{k}\cdot\boldsymbol{r}'}d\boldsymbol{r}' \approx \tilde{\boldsymbol{H}}_q\boldsymbol{\alpha}_q \tag{56}$$

where α_q is the weight of each multipole source for the qth incident field. Because the spectrum of (56) is closer to the local spectrum of the Green function, the less high-frequency information in the contrast source is filtered by the Green function. To convert the high spectrum of contrast with $k_q > k_0$ into the low-passband of the Green function, we have

$$\min_{\boldsymbol{\alpha}_q} \left\|\tilde{\boldsymbol{H}}_q\boldsymbol{\alpha}_q - \tilde{\boldsymbol{g}}_0\right\|_2^2 \tag{57}$$

where $\tilde{\boldsymbol{g}}_0$ is the 2-D-fast Fourier transform (FFT) of the Green function in DOI. Equation (57) can be solved by the conjugate gradient method.

The performance of this method is examined as follows. The DOI is a square with sides of length λ_0, and the measurement curve C is a circle with a radius $3\lambda_0$ whose center is the same as the DOI. Forty sources are equally spaced in the measurement curve. The object spectra k_q are set as $[-6k_0, 6k_0]$. Fig. 3 shows the spectra of the incident fields.

Fig. 3 shows the spectrum of the incident field. Both spectra are normalized and logarithmically transformed with 20log(.). Obviously, the local bandwidth of the optimized incident field is $3k_0$, while the local bandwidth of the uniform excited incident field remains k_0. Fig. 4 depicts the spectrum of corresponding contrast sources.

The spectra of contrast sources in Fig. 4 come from the sum of contrasts with $k_q \in [-6k_0, 6k_0]$ illuminated by uniform excited incident fields and optimized incident fields. Both spectra are normalized and logarithmically transformed with 20log(.). The bandwidth of the contrast source of uniform excited incident fields remains in the range of k_q, while the

bandwidth of the contrast source of optimized incident fields is compressed into k_0. The numerical example shows the ability to keep the spectrum of contrast sources for the contrast with $k_q > k_0$ in the low-passband of the Green function. Applying the incident field optimization for different k_q can retain each part of the wideband spectrum of the contrast, which provides a quantitative method to acquire the high-frequency information of the contrasts.

V. Results and Discussion

In this section, we first compare the performances of CSI, inverse T-matrix, and the new inversion method with and without incident fields optimized. Then, the new inversion method is verified against experimental laboratory-controlled data.

A. Example 1 With Synthetic Data

To assess the resolution performance of the proposed approach, we exploited synthetic data from method of the moments (MOM). The forward problem is solved with the conjugate gradient FFT (CG-FFT) method to acquire the measurement data [54]. Ten percent additive white Gaussian noise (AWGN) is added to the synthetic data for all tests. The first test is employed to compare the reconstruction results with and without incident field optimization. The second test is employed to verify APUM against objects with mixed boundary conditions, of which the result is compared with the results of the normal CSI and inverse T-matrix methods. The third test applied APUM along with the incident field optimized on objects with mixed boundary conditions. The reconstruction errors are quantified by

$$E_{rr} = \left\| \boldsymbol{\chi}_n - \boldsymbol{\chi} \right\|_2 / \left\| \boldsymbol{\chi} \right\|_2. \tag{58}$$

In the first example, we use an E shape dielectric object with width $\lambda_0/3$ and height $3\lambda_0/5$, which has shape edges and small details. Contrast of the objects is 4. The DOI is a square with sides of length λ_0, and the measurement curve C is a circle with radius $3\lambda_0$ whose center is the same as the DOI. Forty transmitters and forty receivers are equally spaced in the measurement curve. The discrete form of the problem is obtained by dividing the DOI into 30×30 subsquares. To avoid inverse crime, the forward problems are calculated with a finer 50×50 grid mesh. Because there are only transmission conditions on the boundaries of objects, APUM reduces to the normal CSI method. The incident fields are optimized with the object contrast spectra k_q set as $[-6k_0, 6k_0]$. In comparison, the incident fields without optimization are excited by one of the 40 sources each time with uniform weighting. According to the results in Fig. 2(a), there are few superoscillation effects in the incident fields excited by 40 sources in turn. Fig. 5 shows the original contrast, the initial values of the contrast sources, and the reconstructed contrasts. The spectra of the sums of contrast sources for the two results are depicted in Fig. 6.

The results with optimized incident fields possess sharper edges than the results with uniform excited incident fields. The corresponding errors of the result with optimization

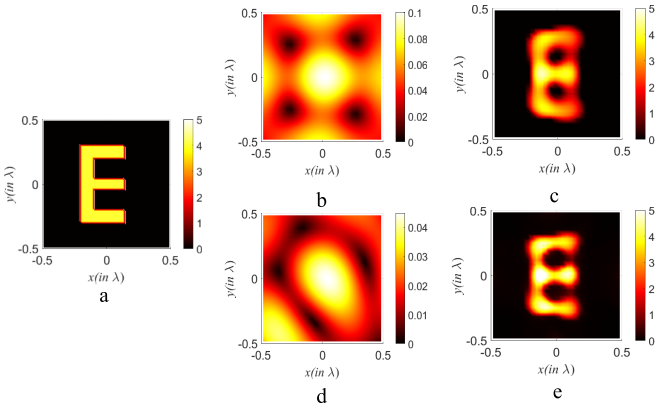

Fig. 5. (a) Original contrast; (b) initial value of the contrast source with uniform incident fields; (c) reconstructed contrast with uniform incident fields; (d) initial value of the contrast source with optimized incident field; and (e) reconstructed contrast with optimized incident field.

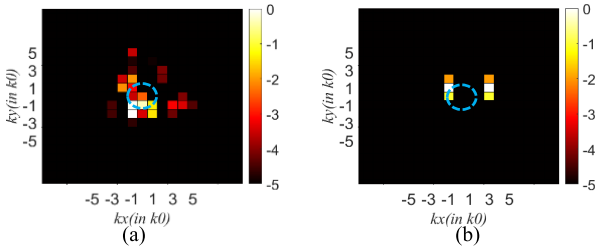

Fig. 6. Spectrum of: (a) contrast sources excited by uniform sources and (b) sum of contrast sources excited by optimized sources.

are smaller than those of the result without optimization. There are significant differences between the initial guess in Fig. 5(b) and (d) and the final results in Fig. 5(c) and (e), which shows that the initial value of the contrast source has little effect on the iteration. The difference among the reconstructed contrast is mainly determined by the difference among the ground truths of the contrast sources, which shows the importance of optimizing the incident fields. The thin cyan dotted lines in Fig. 6 are indications of the low-passband of the Green function. The sum of contrast sources with optimization conserves energy in the low-passband of the Green function, while the sum of contrast sources without optimization has fewer components in the low-passband of the Green function.

To further test the stability of the superoscillation effects, we add Gaussian noise with zero mean at each measurement. The variance of the noise is defined as

$$\sigma_{noise}^2 = \frac{\sum_{m=1}^{M} \left\| \boldsymbol{e}_i^{sca}(m) \right\|^2}{M \cdot SNR} \tag{59}$$

where SNR is the signal-to-noise ratio. The reconstruction errors in iteration with different SNRs are depicted in Fig. 7.

The errors with uniform weighting are higher than the errors with optimized weighting, which shows the regularization effect of superoscillation. However, the errors of optimized weighting with 5 dB SNR raise up after 200 iterations, which shows lack of convergence. On the contrary, the errors of uniform weighting with 5 dB SNR converge to 0.63. Therefore, the superoscillation effect, for the considered case, cannot

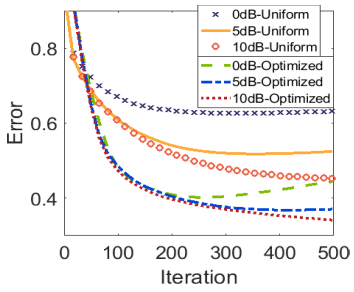

Fig. 7. Reconstruction errors in iterations. The purple line with "x" symbol, the orange line with "o" symbol, and the yellow solid line are the errors with uniform incident fields where the SNRs are 0, 5, and 10 dB, respectively. The green dashed line, the blue dash-dotted line, and the red dotted line are the errors with optimized incident fields where the SNRs are 0, 5, and 10 dB, respectively.

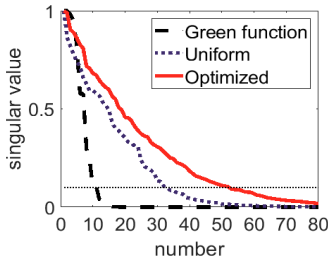

Fig. 8. Example 1: SVD of operators $\boldsymbol{G}_0$ and $\boldsymbol{G}_0\boldsymbol{E}$. The x-axis is the number of singular values and y-axis is the normalized singular value. The black dashed line is the SVD of $\boldsymbol{G}_0$; the blue dotted line is the SVD of $\boldsymbol{G}_0\boldsymbol{E}$ in classical-CSI; the red line is the SVD of $\boldsymbol{G}_0\boldsymbol{E}$ in superoscillation-CSI; and the thin black dotted line is the reference line of 0.1.

work at SNR lower than 5 dB, and that, generally speaking, care should be provided to their use for low SNRs.

For the scattering data linear to the incident fields, the equation with optimized incident fields is a weighted combination of the scattering equation with uniform excited incident fields. The data equation can be rewritten as the operator $\boldsymbol{G}_0\boldsymbol{E}$ mapping the contrast $\boldsymbol{\chi}$ into the data $\boldsymbol{e}_q^{\text{sca}}$. The weighting of the equations enhances the small singular values of operator $\boldsymbol{G}_0\boldsymbol{E}$. The SVDs of $\boldsymbol{G}_0\boldsymbol{E}$ with and without optimization are shown in Fig. 8. The black dotted line indicates the level of noise. As $\boldsymbol{G}_0\boldsymbol{E}$ is a compact operator, the singular values of $\boldsymbol{G}_0\boldsymbol{E}$ converge to zero in both cases. The small singular values below the noise level are unavailable in reconstructions. However, the singular values with the incident field optimized descend slower than those without optimization. Therefore, optimization of incident fields plays a regularization role in the scattering equation.

B. Example 2 With Synthetic Data

To evaluate the capacity of mixed objects imaging, in the second example, we apply APUM to objects consisting of dielectric scatterers and conducting scatterers. A square copper cylinder with a side length $\lambda_0/5$ is wrapped in a circular dielectric cylinder with a radius $2\lambda_0/5$. The conductivity of the copper cylinder is 6×10^7 S/m, and the contrast of dielectric cylinder is 4. The DOI and measurement curve remain the same as those in the first example. Forty transmitters and receivers are equally spaced in the measurement curve. The

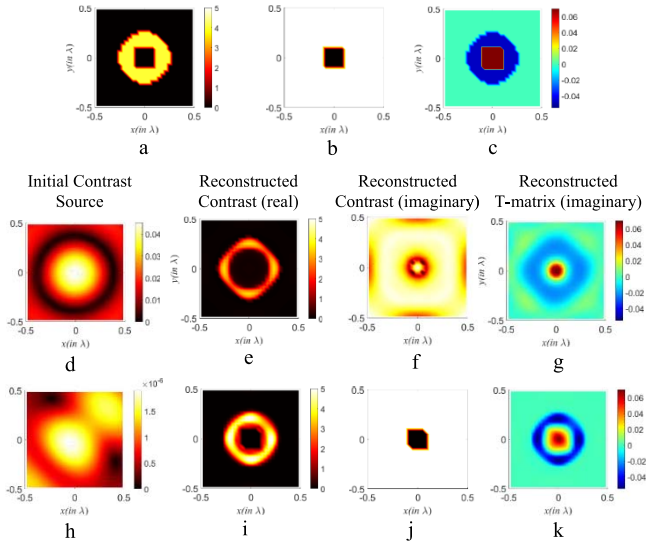

Fig. 9. Example 2: (a) Real part of original contrast; (b) imaginary part of original contrast; and (c) imaginary parts of original T-matrix. (d) Initial value of contrast sources for normal CSI and inverse T-matrix method; (e) and (f) Real and imaginary parts of reconstructed contrast with normal CSI; (g) Imaginary part of reconstructed T-matrix with inverse T-matrix method; (h)–(k) Initial value of the contrast source, real part of reconstructed contrast, imaginary part of reconstructed contrast, and reconstructed T-matrix, respectively, with APUM.

discrete form of the problem is obtained by dividing DOI into 30×30 subsquares. The incident fields are optimized with $k_q \in [-6k_0, 6k_0]$. The reconstructed results with normal CSI, inverse T-matrix, and APUM are shown in Fig. 9.

APUM keeps the sharp edges of the rectangle conducting scatterer in the reconstructed result, while normal CSI fails to reconstruct the conducting scatter and inverse T-matrix obtains the conducting scatterer with blurred contour. The APUM result has a clear boundary between the dielectric scatterers and the conducting scatterers, while both the results from the normal CSI and inverse T-matrix have gaps between the two kinds of scatterers. The large imaginary parts of conducting scatterers ruin the real parts of contrasts in Fig. 9(d) reconstructed by normal CSI. The zero-order multipole expansion in the inverse T-matrix lacks high spectrum information and blurs the reconstructed T-matrix in Fig. 9(f).

The singular values of $\boldsymbol{G}_0\boldsymbol{E}$ with and without optimization are shown in Fig. 10. The singular values with the incident field optimized descend slower than those without optimization.

C. Example 3 With Synthetic Data

To verify the method on real application scenarios, the third example is a safety inspection scene. We modeled the cross section of the human body permittivity image at 900 MHz according to high-resolution axial anatomical images of the male dataset from the Visible Human Dataset, Visible Human Project (NIH, USA). A metal gun is carried against the body, of which the cross section is a rectangle with a size of 12.4 cm $\times$ 3.6 cm.

The DOI is 0.64 m $\times$ 0.64 m and desecrated to 98×98 subunits. The forward problems are calculated with

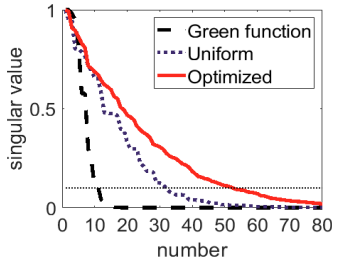

Fig. 10. Example 2: SVD of operators $\boldsymbol{G}_0$ and $\boldsymbol{G}_0\boldsymbol{E}$. The x-axis is the number of singular values and y-axis is the normalized singular value. The black dashed line is the SVD of $\boldsymbol{G}_0$; the blue dotted line is the SVD of $\boldsymbol{G}_0\boldsymbol{E}$ in classical-CSI; the red line is the SVD of $\boldsymbol{G}_0\boldsymbol{E}$ in superoscillation-CSI; and the thin black dotted line is the reference line of 0.1.

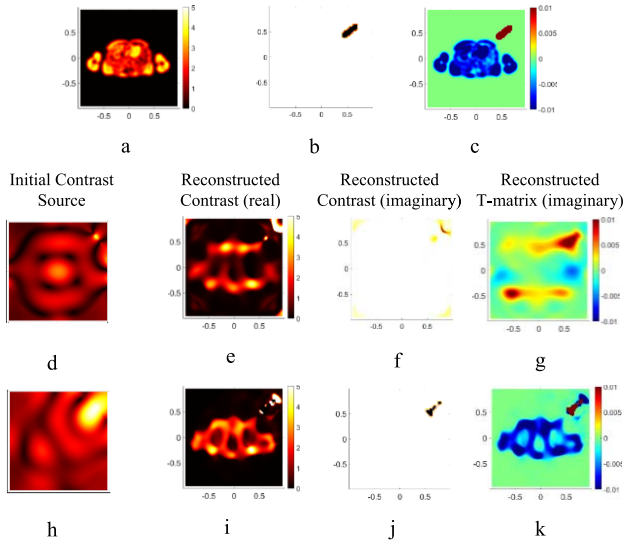

Fig. 11. Example 3: (a) Real part of original contrast; (b) imaginary part of original contrast; and (c) imaginary parts of original T-matrix. (d) Initial value of contrast sources for normal CSI and inverse T-matrix method; (e) and (f) Real and imaginary parts of reconstructed contrast with normal CSI; (g) Imaginary part of reconstructed T-matrix with inverse T-matrix method; (h)–(k) Initial value of the contrast source, real part of reconstructed contrast, imaginary part of reconstructed contrast, and reconstructed T-matrix, respectively, with APUM.

a 262 × 262 grid mesh to avoid inverse crime. Eighty transmitters illuminate the DOI on the circle of radius 1 m, and 80 receivers on the same circle collect the scattering field at each illumination. The incident fields are optimized with $k_q \in [-6k_0, 6k_0]$. The reconstruction results of APUM with optimized incident fields, inverse T-matrix with uniform incident fields, and normal CSI with uniform incident fields are shown in Fig. 11.

The cross section of human body is wavelength scale, which makes normal CSI and inverse T-matrix method fail in reconstruction. By comparison, the APUM result can reconstruct the outline of the body and indicate the weapon. Therefore, APUM with optimization can reconstruct the subwavelength scale scatterers with mixed boundary conditions effectively.

D. Example 4 With Experimental Data

To validate the proposed method against the experimental data, we adopt the experimental dataset collected by Institute Fresnel, Marseille, France [55]. The dataset "FoamMetExt" is

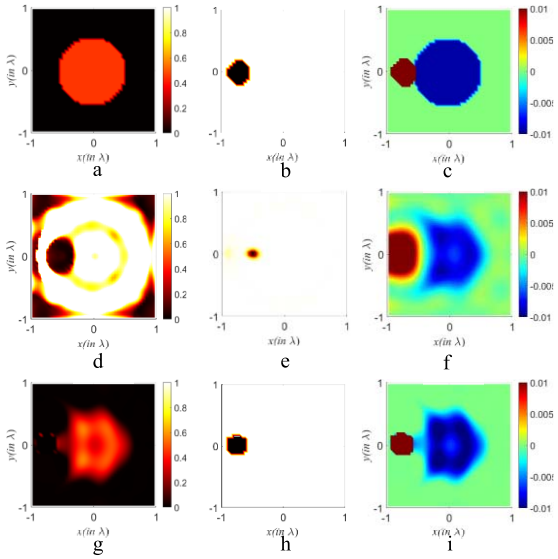

Fig. 12. (a) Real parts of original contrasts; (b) imaginary parts of original contrasts; and (c) imaginary parts of original T-matrix; (d) Real parts of reconstructed contrasts with normal CSI; (e) imaginary parts of reconstructed contrasts with normal CSI; and (f) imaginary parts of reconstructed T-matrix with inverse T-matrix; (g) Real parts of reconstructed contrasts with APUM; (h) imaginary parts of reconstructed contrasts with APUM; and (i) reconstructed conducting T-matrix with APUM.

tested, where a copper cylinder with a radius of 28.5 mm is placed against a foam cylinder with a radius of 80 mm in DOI. The foam cylinder has $\varepsilon_r = 1.45 \pm 0.15$. Eighteen sources illuminate the DOI in turn around a circle with a radius of 1.67 m. The scattering field of each illumination is collected at 241 receiving locations in the circle with a radius 1.67 m. The data are collected at 17 frequencies from 2to 18 GHz.

We use the data at 4 GHz for reconstruction. The DOI is of size 150 mm × 150 mm and discrete as 44 × 44 subsquares. Fig. 12 compares the reconstruction result of APUM with the result of inverse T-matrix, of which the APUM result is better than inverse T-matrix result.

Because of the existence of PEC scatterers with large imaginary part, the normal CSI method fails to reconstruct the scatterers in this configuration. With larger DOI and finer mesh, the normal CSI method can perform better [14]. The result of APUM is also affected by the rough grid, which results in the gap between the PEC scatterer and the dielectric scatterer. Only 4 GHz data are applied in the reconstruction, and the copper cylinder is 0.38λ, which shows the effectiveness of the proposed method handling subwavelength scale objects.

VI. Conclusion

In this article, we proposed a method for the mixed boundary condition ISP. The contrast of the dielectric scatterers and the T-matrix of the PEC scatterers are alternately updated, which avoids the contrast interfered by the large imaginary parts of PEC scatterers and improves the accuracy of the reconstructed T-matrix. The proposed method was verified against synthetic data and experimental data. Compared with APUM, normal CSI is vulnerable to imaginary parts of

conducting scatterers, and the inverse T-matrix lacks high spectrum information for limited multipole expansion orders.

To further improve the resolution, we studied the regularization effects of superoscillatory incident fields and proposed a method to apply these regularization effects to objects with mixed boundary conditions. The superresolution ability of nonlinear inverse scattering is attributed to evanescent-to-propagating wave conversion effects, which is doubted in [9] and [27]. We provided a superresolution method in nonlinear ISP by quantitatively converting the high spatial spectrum of contrasts into low spectrum contrast sources, which can retain the high-frequency information in the low-passband of the Green function. The proposed method achieves similar effects of evanescent-to-propagating wave conversion. The mixing between the local spectrum of the superoscillatory incident field and the spectrum of objects can produce low-spatial frequency contrast sources. With the *a priori* information of incident fields, high-frequency information of objects can be retrieved by solving the nonlinear ISP. Furthermore, the incident field is linear to the scattering data. The scattering data of optimized incident fields can be obtained by weighting the combination of the scattering data of incident fields without optimization. Therefore, the optimization of incident fields is a regularization strategy of the scattering equation. The numerical example shows that the optimization can improve the small singular values of compact operator $\boldsymbol{G}_0\boldsymbol{E}$.

In this article, we focused on the applications that require low-frequency waves to penetrate the imaging area, such as the through wall and ground penetrating imaging. In these practical applications, the scale of region of interest (ROI) is always limited. With given configurations of antenna array and the SNR, the smaller the ROI, the more significant the superoscillation. Therefore, we can start with illuminating the ROI with low-frequency wave carrying strong superoscillation effects. Then, the ROI can be narrowed down according to the result in the first illumination. Then we can further illuminate the new ROI with higher frequency and repeat the last step until the whole ROI filled with objects.

The optimization of incident fields is a general strategy applicable to all ISPs with boundary condition models or volume equivalence models. APUM combines the strength of two models and makes the regularization strategy available for different kinds of objects. APUM with incident field optimization introduces little *a priori* information and achieves much higher resolution.

Further improvements of the inverse algorithm and the use of *a priori* information on this framework are indeed expected.

APPENDIX

In the T-matrix model, the DOI is discretized into N small cylindrical elements at first. The center of the nth elements is $\boldsymbol{r}_n$. The qth incident field is composed of I multipoles with expansion degrees γ ranging from $-\tau$ to $+\tau$

$$\boldsymbol{E}^{inc}(\boldsymbol{r}) = \boldsymbol{u}_z \sum_{i=1}^{I} \sum_{\gamma=-\tau}^{+\tau} a_{\gamma i}(q) H_\gamma^{(2)}(k_0|\boldsymbol{r}-\boldsymbol{r}_i|) e^{j\gamma\varphi(\boldsymbol{r}-\boldsymbol{r}_i)} \quad \text{(A1)}$$

where $a_{\gamma i}$ is the γth expansion of the ith multipole, $\boldsymbol{r}_i$ is the position of the ith multipole, $\varphi(\boldsymbol{r}-\boldsymbol{r}_i)$ is the angle of $\boldsymbol{r}-\boldsymbol{r}_i$ in the cylindrical coordinates, and $H_\gamma^{(2)}$ is the γth order second kind Hankel function. According to Graf's addition theorem, the incident field of the ith multipole is expressed as a multipole expansion on the center of the nth elements

$$\begin{aligned} &H_\gamma^{(2)}(k_0|\boldsymbol{r}-\boldsymbol{r}_i|)e^{j\gamma\varphi(\boldsymbol{r}-\boldsymbol{r}_i)} \\ &\quad = e^{j\gamma\pi}\left[\sum_{p=-\infty}^{+\infty} \begin{matrix} H_{\gamma+p}^{(2)}(k_0|\boldsymbol{r}_i-\boldsymbol{r}_n|)e^{j(\gamma+p)\varphi(\boldsymbol{r}_i-\boldsymbol{r}_n)} \\ J_p(k_0|\boldsymbol{r}-\boldsymbol{r}_n|)e^{-jp\varphi(\boldsymbol{r}-\boldsymbol{r}_n)} \end{matrix}\right] \end{aligned} \quad \text{(A2)}$$

where J_p is the pth order Bessel function. The corresponding multipole expansion of the scattering field outside the nth cylinder can be expressed as

$$\begin{aligned} &\boldsymbol{E}^{sca}(\boldsymbol{r}-\boldsymbol{r}_n) \\ &= \boldsymbol{u}_z \sum_{p=-\infty}^{+\infty} \left[c_{np}(q) H_p^{(2)}(k_0|\boldsymbol{r}-\boldsymbol{r}_n|)e^{-jp\varphi(\boldsymbol{r}-\boldsymbol{r}_n)}\right] \\ &\quad + \sum_{\substack{n'=1 \\ n'\neq n}}^{N} \sum_{p=-\infty}^{+\infty} \left[c_{n'p}(q) \sum_{l=-\infty}^{+\infty} \begin{matrix} H_{p+l}^{(2)}(k_0|\boldsymbol{r}_n-\boldsymbol{r}_{n'}|) \\ \times e^{-j(p+l)\varphi(\boldsymbol{r}_n-\boldsymbol{r}_{n'})} \\ J_l(k_0|\boldsymbol{r}-\boldsymbol{r}_n|)e^{jl\varphi(\boldsymbol{r}-\boldsymbol{r}_n)}e^{-jp\pi} \end{matrix}\right] \end{aligned} \quad \text{(A3)}$$

where c_{np} is the unknown pth order scattering coefficient of the nth element. The transmitting field inside the nth cylinder is given by

$$\boldsymbol{E}^{tran}(\boldsymbol{r}) = \boldsymbol{u}_z \sum_{p=-\infty}^{+\infty} b_{np}(q) J_p(k_n|\boldsymbol{r}-\boldsymbol{r}_n|)e^{-jp\varphi(\boldsymbol{r}-\boldsymbol{r}_n)} \quad \text{(A4)}$$

where b_{np} is the unknown pth order transmitting coefficient of the n th element, and k_n is the wavenumber inside the nth element.

Therefore, the transmitting boundary condition on the surface of the nth element with radius R can be expressed as

$$\left[\boldsymbol{E}^{inc}(\boldsymbol{r}) + \boldsymbol{E}^{sca}(\boldsymbol{r})\right]_{|\boldsymbol{r}-\boldsymbol{r}_n|=R} = \boldsymbol{E}^{trans}(\boldsymbol{r})\big|_{|\boldsymbol{r}-\boldsymbol{r}_n|=R} \quad \text{(A5)}$$

while the right components of (A5) are zero in the PEC scatterers. The corresponding boundary condition of the magnetic field for the nth element is obtained from the electric field as

$$\left[\frac{\partial \boldsymbol{E}^{inc}(\boldsymbol{r})}{\partial r} + \frac{\partial \boldsymbol{E}^{sca}(\boldsymbol{r})}{\partial r}\right]_{|\boldsymbol{r}-\boldsymbol{r}_n|=R} = \left.\frac{\partial \boldsymbol{E}^{trans}(\boldsymbol{r})}{\partial r}\right|_{|\boldsymbol{r}-\boldsymbol{r}_n|=R}. \quad \text{(A6)}$$

Solving (A5) and (A6) along with the orthogonal property of $\exp[-jp\varphi(\boldsymbol{r}-\boldsymbol{r}_n)]$, we obtain the pth order of the scattering coefficients from the nth element

$$\begin{aligned} &J_p(k_0R)\sum_{i=1}^{I}\sum_{\gamma=-\Gamma}^{+\Gamma}\left[\begin{matrix} a_{\gamma i}H_{\gamma+p}^{(2)}(k_0|\boldsymbol{r}_i-\boldsymbol{r}_n|) \\ e^{j\gamma\pi}e^{j(p+\gamma)\varphi(\boldsymbol{r}_i-\boldsymbol{r}_n)} \end{matrix}\right] \\ &\quad + J_{-p}(k_0R)\sum_{\substack{n'=1 \\ n'\neq n}}^{N}\sum_{p'=-\infty}^{+\infty}\left[\begin{matrix} c_{n'p'}H_{p'-p}^{(2)}(k_0|\boldsymbol{r}_n-\boldsymbol{r}_{n'}|) \\ e^{-jp'\pi}e^{j(p-p')\varphi(\boldsymbol{r}_n-\boldsymbol{r}_{n'})} \end{matrix}\right] \\ &\quad + c_{np}H_p^{(2)}(k_0R) = b_{np}J_p(k_nR) \end{aligned} \quad \text{(A7)}$$

and

$$J_p'(k_0R)\sum_{i=0}^{I}\sum_{\gamma=-\Gamma}^{+\Gamma}\begin{bmatrix} a_{\gamma i}H_{\gamma+p}^{(2)}(k_0|\boldsymbol{r}_i-\boldsymbol{r}_n|) \\ e^{j\gamma\pi}e^{j(p+\gamma)\varphi(\boldsymbol{r}_i-\boldsymbol{r}_n)}\end{bmatrix} + J_{-p}'(k_0R)\sum_{\substack{n'=1\\n'\neq n}}^{N}\sum_{p'=-\infty}^{+\infty}\begin{bmatrix} c_{n'p}H_{p'-p}^{(2)}(k_0|\boldsymbol{r}_n-\boldsymbol{r}_{n'}|) \\ e^{-jp'\pi}e^{j(p-p')\varphi(\boldsymbol{r}_n-\boldsymbol{r}_{n'})}\end{bmatrix} + c_{np}H_p^{(2)'}(k_0R) = \frac{k_n}{k_0}b_{np}J_p'(k_nR). \tag{A8}$$

Introducing (A7) into (A8), we have

$$c_{np} = t_n^p\left[i_n^p + \sum_{n'=1}^{N}\sum_{p'=-\infty}^{+\infty}s_{n,n'}^{p,p'}\left(1-\delta_{n,n'}\right)c_{n'p'}\right] \tag{A9}$$

where

$$\delta_{n,n'} = \begin{cases} 0, & n\neq n' \\ 1, & n=n'\end{cases} \tag{A10}$$

$$s_{n,n'}^{p,p'} = e^{j(p-p')\pi}H_{p'-p}^{(2)}(k_0|\boldsymbol{r}_n-\boldsymbol{r}_{n'}|)e^{j(p-p')\varphi(\boldsymbol{r}_n-\boldsymbol{r}_{n'})} \tag{A11}$$

and

$$i_n^p(q) = \sum_{i=1}^{I}\sum_{\gamma=-\tau}^{+\tau}\begin{matrix}\alpha_{\gamma i}(q)e^{j\gamma\pi}e^{j(\gamma+p)\varphi(\boldsymbol{r}_i-\boldsymbol{r}_n)} \\ H_{\gamma+p}^{(2)}(k_0|\boldsymbol{r}_i-\boldsymbol{r}_n|).\end{matrix} \tag{A12}$$

The element with the dielectric boundary condition has the parameter

$$t_n^p = \frac{k_nJ_p(k_0R)J_{p+1}(k_nR)-k_0J_p(k_nR)J_{p+1}(k_0R)}{k_0J_p(k_nR)H_{p+1}^{(2)}(k_0R)-k_nH_p^{(2)}(k_0R)J_{p+1}(k_nR)} \tag{A13}$$

while the element with the PEC boundary condition has the parameter

$$t_n^p = -\frac{J_p(k_0R)}{H_p^{(2)}(k_0R)}. \tag{A14}$$

REFERENCES

[1] F. Ben Hassen, Y. Boukari, and H. Haddar, "Application of the linear sampling method to identify cracks with impedance boundary conditions," *Inverse Problems Sci. Eng.*, vol. 21, no. 2, pp. 210–234, Mar. 2013.

[2] M. Benedetti, M. Donelli, A. Martini, M. Pastorino, A. Rosani, and A. Massa, "An innovative microwave-imaging technique for nondestructive evaluation: Applications to civil structures monitoring and biological bodies inspection," *IEEE Trans. Instrum. Meas.*, vol. 55, no. 6, pp. 1878–1884, Dec. 2006.

[3] L. M. Neira, B. D. Van Veen, and S. C. Hagness, "High-resolution microwave breast imaging using a 3-D inverse scattering algorithm with a variable-strength spatial prior constraint," *IEEE Trans. Antennas Propag.*, vol. 65, no. 11, pp. 6002–6014, Nov. 2017.

[4] T. U. Gurbuz, B. Aslanyurek, E. P. Karabulut, and I. Akduman, "An efficient nonlinear imaging approach for dielectric objects buried under a rough surface," *IEEE Trans. Geosci. Remote Sens.*, vol. 52, no. 5, pp. 3013–3022, May 2014.

[5] Y. Chu *et al.*, "Fast microwave through wall imaging method with inhomogeneous background based on Levenberg–Marquardt algorithm," *IEEE Trans. Microw. Theory Techn.*, vol. 67, no. 3, pp. 1138–1147, Mar. 2019.

[6] L. D. Donato and L. Crocco, "Model-based quantitative cross-borehole GPR imaging via virtual experiments," *IEEE Trans. Geosci. Remote Sens.*, vol. 53, no. 8, pp. 4178–4185, Aug. 2015.

[7] F. C. Chen and W. C. Chew, "Experimental verification of super resolution in nonlinear inverse scattering," *Appl. Phys. Lett.*, vol. 72, no. 23, pp. 3080–3082, Jun. 1998.

[8] T. J. Cui, W. C. Chew, X. X. Yin, and W. Hong, "Study of resolution and super resolution in electromagnetic imaging for half-space problems," *IEEE Trans. Antennas Propag.*, vol. 52, no. 6, pp. 1398–1411, Jun. 2004.

[9] X. Chen, *Computational Methods for Electromagnetic Inverse Scattering*. Hoboken, NJ, USA: Wiley, 2018.

[10] A. Kirsch, "The MUSIC-algorithm and the factorization method in inverse scattering theory for inhomogeneous media," *Inverse Problems*, vol. 18, no. 4, pp. 1025–1040, 2002.

[11] D. Colton, H. Haddar, and M. Piana, "The linear sampling method in inverse electromagnetic scattering theory," *Inverse Problems*, vol. 19, no. 6, pp. 105–137, 2003.

[12] N. Vojnovic, M. Nikolic Stevanovic, L. Crocco, and A. R. Djordjevic, "High-order sparse shape imaging of PEC and dielectric targets using TE polarized fields," *IEEE Trans. Antennas Propag.*, vol. 66, no. 4, pp. 2035–2043, Apr. 2018.

[13] L. Crocco, M. D'Urso, and T. Isernia, "Testing the contrast source extended Born inversion method against real data: The TM case," *Inverse Problems*, vol. 21, no. 6, pp. 33–50, 2005.

[14] C. Yu, L. P. Song, and Q. H. Liu, "Inversion of multi-frequency experimental data for imaging complex objects by a DTA–CSI method," *Inverse Problems*, vol. 21, no. 6, pp. 165–178, 2005.

[15] X. Ye, X. Chen, Y. Zhong, and R. Song, "Simultaneous reconstruction of dielectric and perfectly conducting scatterers via T-matrix method," *IEEE Trans. Antennas Propag.*, vol. 61, no. 7, pp. 3774–3781, Jul. 2013.

[16] P. C. Waterman, "Matrix formulation of electromagnetic scattering," *Proc. IEEE*, vol. 53, no. 8, pp. 805–811, Aug. 1965.

[17] G. P. Otto and W. C. Chew, "Microwave inverse scattering—Local shape function imaging for improved resolution of strong scatterers," *IEEE Trans. Microw. Theory Techn.*, vol. 42, no. 1, pp. 137–141, Jan. 1994.

[18] G. P. Otto and W. C. Chew, "Inverse scattering of H_z waves using local shape-function imaging: A T-matrix formulation," *Int. J. Imag. Syst. Technol.*, vol. 5, no. 1, pp. 22–27, 1994.

[19] R. Song, X. Ye, and X. Chen, "Reconstruction of scatterers with four different boundary conditions by T-matrix method," *Inverse Problems Sci. Eng.*, vol. 23, no. 4, pp. 601–616, May 2015.

[20] W. C. Chew, *Waves and Fields in Inhomogeneous Media*. New York, NY, USA: Van Nostrand Reinhold, 1990.

[21] A. Kirsch, *An Introduction to the Mathematical Theory of Inverse Problems*. New York, NY, USA: Springer-Verlag, 1996.

[22] O. M. Bucci and G. Franceschetti, "On the degrees of freedom of scattered fields," *IEEE Trans. Antennas Propag.*, vol. 37, no. 7, pp. 918–926, Jul. 1989.

[23] M. A. Maisto, R. Solimene, and R. Pierri, "Resolution limits in inverse source problem for strip currents not in Fresnel zone," *J. Opt. Soc. Amer. A, Opt. Image Sci.*, vol. 36, no. 5, pp. 826–833, May 2019.

[24] A. Abubaker and P. M. V. D. Berg, "Total variation as a multiplicative constraint for solving inverse problems," *IEEE Trans. Image Process.*, vol. 10, no. 9, pp. 1384–1392, Sep. 2001.

[25] K. Xu, Y. Zhong, R. Song, X. Chen, and L. Ran, "Multiplicative-regularized FFT twofold subspace-based optimization method for inverse scattering problems," *IEEE Trans. Geosci. Remote Sens.*, vol. 53, no. 2, pp. 841–850, Feb. 2015.

[26] G. Oliveri, P. Rocca, and A. Massa, "A Bayesian compressive sampling based inversion for imaging sparse scatterers," *IEEE Trans. Geosci. Remote Sens.*, vol. 49, no. 10, pp. 3993–4006, Oct. 2011.

[27] S. Sun, B. J. Kooij, and A. G. Yarovoy, "Linearized 3-D electromagnetic contrast source inversion and its applications to half-space configurations," *IEEE Trans. Geosci. Remote Sens.*, vol. 55, no. 6, pp. 3475–3487, Jun. 2017.

[28] G. Oliveri, L. Poli, N. Anselmi, M. Salucci, and A. Massa, "Compressive sensing-based Born iterative method for tomographic imaging," *IEEE Trans. Microw. Theory Techn.*, vol. 67, no. 5, pp. 1753–1765, May 2019.

[29] W. C. Chew and Y. M. Wang, "An iterative solution of the two-dimensional electromagnetic inverse scattering problem," *Int. J. Imag. Syst. Technol.*, vol. 1, pp. 100–108, Jan. 1989.

[30] P. M. van den Berg and R. E. Kleinman, "A contrast source inversion method," *Inverse Problems*, vol. 13, no. 6, pp. 1607–1620, 1997.

[31] L. Crocco, I. Catapano, L. D. Donato, and T. Isernia, "The linear sampling method as a way to quantitative inverse scattering," *IEEE Trans. Antennas Propag.*, vol. 60, no. 4, pp. 1844–1853, Apr. 2012.

[32] Y. Zhong, M. Lambert, D. Lesselier, and X. Chen, "A new integral equation method to solve highly nonlinear inverse scattering problems," *IEEE Trans. Antennas Propag.*, vol. 64, no. 5, pp. 1788–1799, May 2016.

[33] F. Simonetti, "Multiple scattering: The key to unravel the subwavelength world from the far-field pattern of a scattered wave," *Phys. Rev. E, Stat. Phys. Plasmas Fluids Relat. Interdiscip. Top.*, vol. 73, Art. no. 036619.

[34] K. Belkebir, P. C. Chaumet, and A. Sentenac, "Influence of multiple scattering on three-dimensional imaging with optical diffraction tomography," *J. Opt. Soc. Amer. A, Opt. Image Sci.*, vol. 32, no. 3, pp. 586–595, Mar. 2006.
[35] M. E. Testorf and M. A. Fiddy, "Superresolution imaging—Revisited," *Adv. Imag. Electron Phys.*, vol. 163, no. 10, pp. 165–218, 2010.
[36] N. K. Nikolova, *Introduction to Microwave Imaging (EuMA High Frequency Technologies Series)*. Cambridge, U.K.: Cambridge Univ. Press, Jul. 2017.
[37] R. Pierri, F. Soldovieri, A. Liseno, and F. D. Blasio, "Dielectric profiles reconstruction via the quadratic approach in 2-D geometry from multifrequency and multifrequency/multiview data," *IEEE Trans. Geosci. Remote Sens.*, vol. 40, no. 12, pp. 2709–2718, Dec. 2002.
[38] V. A. Markel, "Investigation of the effect of super-resolution in nonlinear inverse scattering," *Phys. Rev. E, Stat. Phys. Plasmas Fluids Relat. Interdiscip. Top.*, vol. 102, no. 5, Nov. 2020, Art. no. 053313.
[39] J. B. Pendry, "Negative refraction makes a perfect lens," *Phys. Rev. Lett.*, vol. 85, no. 18, pp. 3966–3969, Oct. 2000.
[40] M. Memarian and G. V. Eleftheriades, "Evanescent-to-propagating wave conversion in sub-wavelength metal-strip gratings," *IEEE Trans. Microw. Theory Techn.*, vol. 60, no. 12, pp. 3893–3907, Dec. 2012.
[41] V. Okhmatovski, J. Aronsson, and L. Shafai, "A well-conditioned non-iterative approach to solution of the inverse problem," *IEEE Trans. Antennas Propag.*, vol. 60, no. 5, pp. 2418–2430, May 2012.
[42] W. X. Jiang *et al.*, "Broadband all-dielectric magnifying lens for far-field high-resolution imaging," *Adv. Mater.*, vol. 25, no. 48, pp. 6963–6968, 2013.
[43] L. Wang, L. Li, Y. Li, H. C. Zhang, and T. J. Cui, "Single-shot and single-sensor high/super-resolution microwave imaging based on metasurface," *Sci. Rep.*, vol. 6, no. 1, Jun. 2016, Art. no. 026959.
[44] M. Anzan-Uz-Zaman, K. Song, D. G. Lee, and S. Hur, "A novel approach to Fabry–Pérot-resonance-based lens and demonstrating deep-subwavelength imaging," *Sci. Rep.*, vol. 10, Jul. 2020, Art. no. 010769.
[45] A. Kempf, "Black holes, bandwidths and Beethoven," *J. Math. Phys.*, vol. 41, pp. 2360–2374, Apr. 2000.
[46] F. M. Huang and N. I. Zheludev, "Super-resolution without evanescent waves," *Nano Lett.*, vol. 9, no. 3, pp. 1249–1254, Jan. 2009.
[47] A. M. H. Wong and G. V. Eleftheriades, "Sub-wavelength focusing at the multi-wavelength range using superoscillations: An experimental demonstration," *IEEE Trans. Antennas Propag.*, vol. 59, no. 12, pp. 4766–4776, Dec. 2011.
[48] R. K. Amineh and G. V. Eleftheriades, "2D and 3D sub-diffraction source imaging with a superoscillatory filter," *Opt. Exp.*, vol. 21, no. 7, pp. 8142–8157, Mar. 2013.
[49] A. M. H. Wong and G. V. Eleftheriades, "Broadband superoscillation brings a wave into perfect three-dimensional focus," *Phys. Rev. B, Condens. Matter*, vol. 95, no. 7, Feb. 2017, Art. no. 075148.
[50] G. Gbur, "Using superoscillations for superresolved imaging and sub-wavelength focusing," *Nanophotonics*, vol. 8, no. 2, pp. 205–225, Nov. 2018.
[51] A. M. H. Wong and G. V. Eleftheriades, "Adaptation of Schelkunoff's superdirective antenna theory for the realization of superoscillatory antenna arrays," *IEEE Antennas Wireless Propag. Lett.*, vol. 9, pp. 315–318, 2010.
[52] P. J. S. G. Ferreira and A. Kempf, "Superoscillations: Faster than the Nyquist rate," *IEEE Trans. Signal Process.*, vol. 54, no. 10, pp. 3732–3740, Oct. 2006.
[53] L. Li, F. Li, and T. J. Cui, "Computational superoscillation imaging beyond the Rayleigh limit from far-field measurements," *Opt. Exp.*, vol. 22, no. 5, pp. 5431–5441, Mar. 2014.
[54] P. Zwamborn and P. M. van den Berg, "The three dimensional weak form of the conjugate gradient FFT method for solving scattering problems," *IEEE Trans. Microw. Theory Techn.*, vol. 40, no. 9, pp. 1757–1766, Sep. 1992.
[55] J.-M. Geffrin, P. Sabouroux, and C. Eyraud, "Free space experimental scattering database continuation: Experimental set-up and measurement precision," *Inverse Problems*, vol. 21, no. 6, pp. 117–130, 2005.

Fan Yin (Student Member, IEEE) was born in Hefei, Anhui, China, in 1995. He received the B.S. degree in electronic information engineering from Anhui University, Hefei, in 2016. He is currently pursuing the Ph.D. degree in electronic science and technology with the University of Science and Technology of China, Hefei.

His research interests include inverse scattering problem, near-field microwave imaging, and microwave metamaterials.

Chang Chen (Member, IEEE) received the B.S., M.S., and Ph.D. degrees from the University of Science and Technology of China (USTC), Hefei, China, in 2002, 2005, and 2012, respectively.

He is currently an Associate Professor with the School of Information Science and Technology, USTC. He has considerable experience in antenna design, microwave imaging, and microwave passive components. His current interests include microwave antennas, microwave metamaterials, electromagnetic spectrum sensing, and passive radar.

Weidong Chen (Member, IEEE) received the B.S. degree in electronic engineering from the University of Electronic Science and Technology of China, Chengdu, China, in 1990, and the M.Eng. and Ph.D. degrees in electromagnetic field and microwave technology from the University of Science and Technology of China (USTC), Hefei, China, in 1994 and 2005, respectively.

He is currently a Professor with the Department of Electronic Engineering, USTC, where he is also the Deputy Dean of the School of Information Science and Technology. His research interests are in the areas of microwave imaging theory with applications to radar.